ADVANCED MATERIALS

Supporting Information

for *Adv. Mater.,* DOI: 10.1002/adma.202102232

Wafer-Scale Functional Metasurfaces for Mid-Infrared Photonics and Biosensing

*Aleksandrs Leitis, Ming Lun Tseng, Aurelian John-Herpin, Yuri S. Kivshar, and Hatice Altug**

Supporting information

Wafer-scale functional metasurfaces for mid-infrared photonics and biosensing

Aleksandrs Leitis[1], Ming-Lun Tseng[1], Aurelian John-Herpin[1], Yuri S. Kivshar[2], and Hatice Altug[1]

[1] Institute of Bioengineering, École Polytechnique Fédérale de Lausanne (EPFL), Lausanne 1015, Switzerland

[2] Nonlinear Physics Centre, Australian National University, Canberra ACT 2601, Australia

Effective refractive index and tunability

An essential aspect of the metasurfaces is the effective refractive index of the surrounding medium. A lower and more uniform refractive index of the surrounding medium leads to improved metasurface efficiencies[1,2]. Here we demonstrate that the thin free-standing membranes can lower the effective refractive index when compared to bulk substrates. Figure S1a shows the elliptical meta-atoms in a uniform medium with refractive index n_{medium}. The meta-atom design is based on two elliptically shaped germanium meta-atoms that are slightly tilted compared to the x and y-axis by 20°, see Figure S1a. The germanium has near-zero absorption losses in the mid-IR wavelength range, while the specific asymmetric resonator shape reduces the scattering losses. Such a design supports bound states in continuum[3], therefore providing high-Q resonances. The transmittance spectra for different refractive indexes of the surrounding medium is displayed in Figure S1b. The resonance frequencies for different refractive indexes are shown in Figure S1c. When the meta-atoms are placed on a 100 nm thick Al_2O_3 membrane, the resonance is shifted from 5.85 μm to 6.01 μm wavelength, which corresponds to an effective refractive index of 1.039.

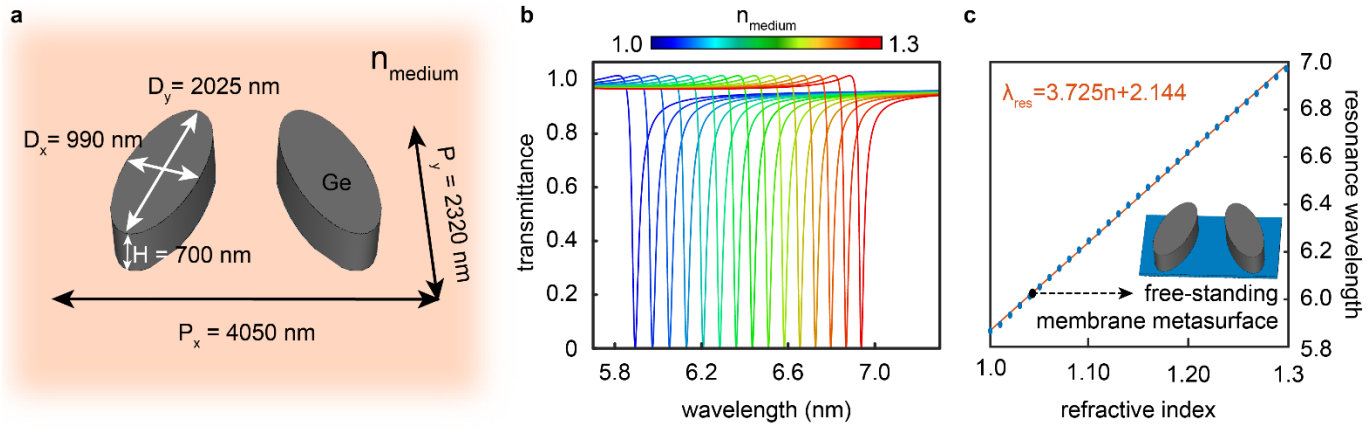

Figure S1: effective refractive index. a) Metasurface unit-cell in a uniform medium **b**) transmittance spectra of the metasurface for different refractive indexes of the medium. **c**) Resonance wavelength for the different refractive indexes of the surrounding medium and when a metasurface is placed on a 100 nm thick Al_2O_3 membrane.

DUV lithography mask layout

The mask for the DUV lithography step was realized on a chrome-coated 6-inch (150 mm) quartz reticle. The metasurface patterns on the DUV mask were produced with a direct laser writing process (Heidelberg Instruments VPG200), which has the capability to realize structures with a minimal feature size of 0.5 µm. Due to the 4x demagnification of the DUV projection system, the patterns on the mask are 4x larger than the final meta-atom dimensions on the wafers. The large available area on the DUV mask allowed to write all the metasurface patterns demonstrated in the main text and the supporting information. Figure S2a shows the DUV lithography mask with three highlighted regions, which were used for nanofabrication of metasurfaces, while the last region which is not highlighted with color shading was not used in the manuscript. The patterns corresponding to each area were projected on separate wafers. The red region in Figure S2a contains 13 regions with high-Q metasurface patterns, see Figure S2b. The highlighted region with a solid line in Figure S2b has metasurface patterns demonstrated in Figure 2 of the main text and Figure S7, while the area highlighted with a dashed line contains the high-Q metasurface design shown in Figure S6. The inset of Figure S2b shows one of the high-Q elliptical meta-atom geometries on the DUV mask. These two metasurface designs were chosen, because it enables a direct comparison between the performance with the previously demonstrated metasurfaces by Tittl *et al*.,[4] and Leitis *et al*.,[5] which were fabricated using EBL processes. The high-Q metasurfaces in Figure 2 of the main text were realized on wafers having a germanium film with a thickness of 700 nm deposited with electron beam evaporation method.

The blue region of the DUV mask has various wavefront shaping and polarization control metasurface designs. The highlighted region with dashed line in Figure S2c indicates the metalens pattern

corresponding to Figures 3b-d of the main text, while the region with the solid line shows the metasurface pattern which was used for birefringent metasurface realization corresponding to Figures 3f and 3g of the main text. The inset of Figure S2c shows part of the metalens pattern on the DUV mask. The wavefront shaping metasurfaces were realized on wafers with a sputtered Ge layer with a thickness of 3.5 µm.

The green area of the DUV mask in Figure S2a contains plasmonic metasurface designs, where the patterns corresponding to the highlighted region with a solid line were used for the experiments demonstrated in Figure 4 of the main text. The inset of Figure S2d shows the multiresonant nanoantenna design realized on the DUV mask. The multiresonant plasmonic metasurfaces were realized on wafers with 100nm thick aluminum film deposited with electron beam evaporation process.

From the insets of Figures S2b and S2c, it is visible that the patterns having round shapes are very well reproduced, while the rectangular designs in Figure S2d are not perfectly reproduced and have rounded corners. The rounded corners of the rectangular patterns can be associated with the resolution limitation of the direct laser writing system, which can achieve minimum feature sizes of 0.5 µm. The consequence of the mask imperfections can be seen in Figure 4b of the main text, where the SEMs of the plasmonic metasurface also show rounded corners of the final nanoantennas on the wafer. The rectangular shapes could be reproduced with a significantly higher precision if the DUV mask was patterned with a high-resolution electron beam lithography process instead of direct laser writing method.

However, when considering smaller dimensions of meta-atoms, the point spread function of the DUV lithography optical projection system would be the limiting factor of the attainable resolution and meta-atom reproduction. While gratings with a pitch size of 150 nm can be realized, achieving sharp edges and corners with DUV lithography process is challenging. The resolution limitations of the high-throughput DUV lithography processes could be overcome with nanoimprint fabrication process[6] or the emerging extreme ultraviolet lithography processes.

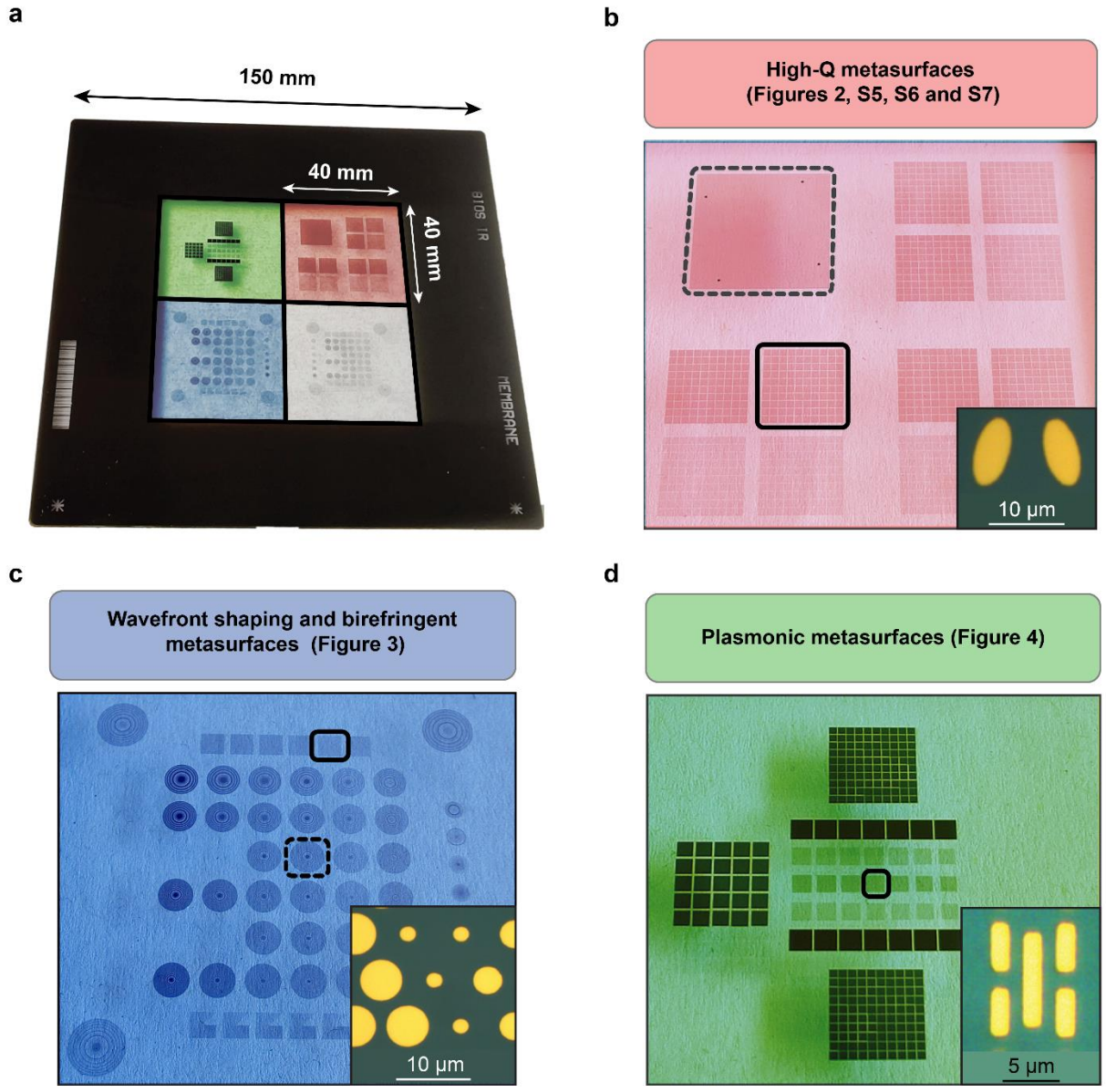

Figure S2: DUV lithography mask layout. a) DUV mask made on 6-inch quartz plate with high-Q, wavefront shaping, and plasmonic metasurface patterns, which were used to realize the metasurfaces demonstrated in Figures 2-4 of the main text. **b**) Mask region containing various high-Q metasurface designs. Highlighted regions indicate the metasurface patterns used in Figures 2, S5, S6, and S7. **c**) Region of the DUV mask with different wavefront shaping and polarization control metasurface patterns. Highlighted regions indicate the metasurface patterns used in Figure 3. **d**) DUV mask region containing various plasmonic metasurface designs, where the highlighted region indicates the metasurface used in Figure 4 of the main text.

High-Q metasurface chip layout

The fabricated high-Q metasurface chip (10 x 10 mm) has 13 different regions with various types of metasurface designs, including tilted elliptical antennas (Figure S3a). Twelve regions consist of 10 x 10 pixelated metasurfaces, where the scaling factor of the unit cell is varied from one ‘metapixel’ to

another (Figure S3b). The last region of the chip consists of a large area metasurface (14 x 14 ‘metapixels’) with uniform resonator size from one ‘metapixel’ to another.

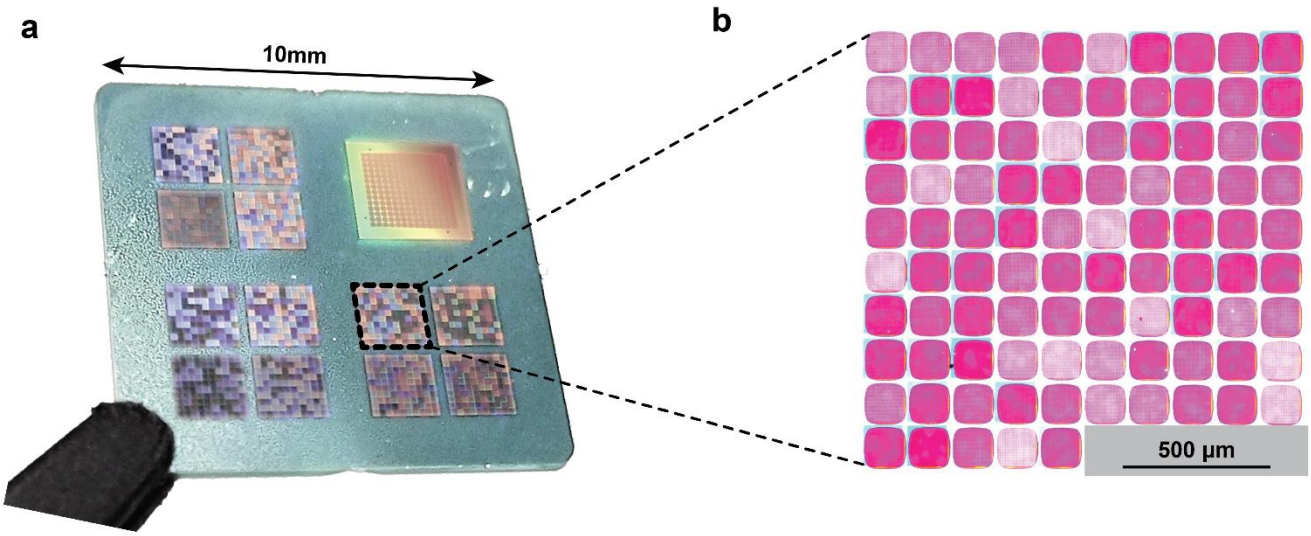

Figure S3: High-Q metasurface chip layout. a) The fabricated chip containing multiple high-Q dielectric metasurfaces. **b**) Pixelated metasurface containing 100 metapixels.

Numerical simulations of High-Q metasurfaces

The precise meta-atom geometry shown in Figure 2 of the main text is displayed in Figure S4a. The metapixel consists of meta-atoms that are arranged in an array over an area of 100 x 100 µm (Figure S4a). We scale the meta-atom size from one metapixel to another while keeping the height of the meta-atoms constant, which allows gradual tuning of the resonance frequencies of the metapixels, see Figure S4b. We randomly shuffled the metapixels with different scaling factors to create 10 x 10 pixelated metasurface, where the distance between the metapixels is 30 µm (Figure S4c). With this pixelated metasurface approach, we can perform direct translation between spectral to spatial information.[4]

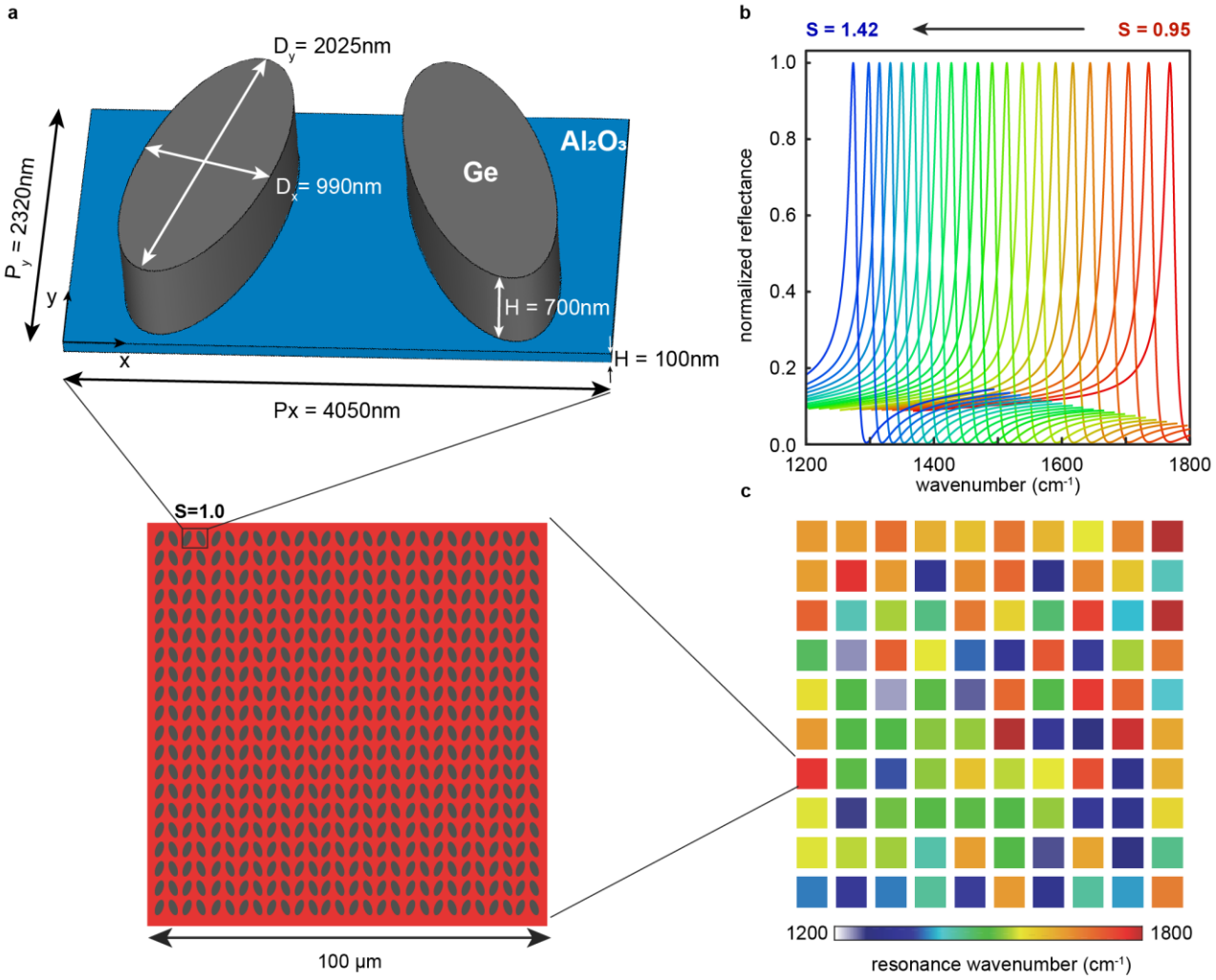

Figure S4: Numerical simulations of membrane-based all-dielectric high-Q metasurfaces. a) Sketch of the meta-atom and a single metapixel. **b**) The simulated reflectance spectra of a representative 22 different high-Q metapixels on a free-standing Al_2O_3 membrane at different scaling factors. **c**) Resonance wavenumber map of the 10 x 10 pixelated metasurface.

Simulation and experimental data comparison of high-Q metasurfaces

In order to compare the measurement data with the simulation results of the high-Q metasurfaces we acquired SEM images of the fabricated elliptically shaped meta-atoms, see the inset of Figure S5. The measured size of the resonator unit cell was 1876 nm for the long ellipse axis, 918 nm for the short ellipse axis, and the x-periodicity of 3753 nm and y-periodicity of 2168 nm. The optical measurement data shows a pronounced reflectance peak at 1746.5 cm^{-1}, while the simulated spectra of the meta-atom arrays with the same dimensions show a resonance peak at 1742.4 cm^{-1} (Figure S5). The measured quality factor of the resonance is 114, while the simulation data show a quality factor of 136. The differences of the resonance peak positions and resonance quality factors between the simulation and experimental data could be explained by a slightly lower refractive index of the evaporated Ge thin films and higher material losses, which broadens the resonances. Additionally, the resonance quality factor of the measurement data could be affected by the thin residues of the photoresist.

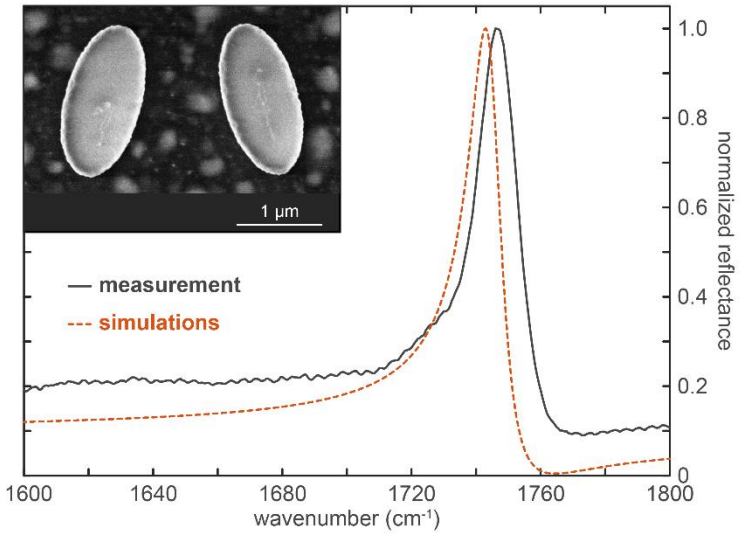

Figure S5: High-Q metasurface measurement and simulation comparison. Inset: SEM of the corresponding meta-atom.

Metasurface uniformity and resonance experimental quality factor

In order to compare the fabricated metasurface uniformity and resonance quality factor, we realized a slightly modified design of the elliptical resonators compared to the ones shown in Figures S4, S5, and Figure 2 of the main text. Here the meta-atom geometry parameters match the ones from the work of Leitis et al.[5], where such germanium-based metasurfaces were realized on CaF_2 substrates using EBL. The dimensions of the experimentally characterized meta-atom are displayed in Figure S6a, where the elliptical resonator is 950 nm wide and 2370 nm long with 4080 nm periodicity along the x-axis and 2380 nm along with 10-degree tilt angle. The precise shape and uniformity of the fabricated metasurface are confirmed with an SEM image (Figure S6b). It shows not only the high-

resolution of the DUV lithography process but also illustrates that we can reliably produce metasurfaces with small gap sizes (~150 nm) between the meta-atoms, which is crucial for improved near-field enhancements. The measured reflectance spectra of the fabricated metasurface are displayed in Figure S6c. The achieved resonance quality factor at normal light incidence angle reaches up to 125, which is comparable to the quality factors of EBL fabricated metasurfaces reported by Leitis *et al.*.[5]

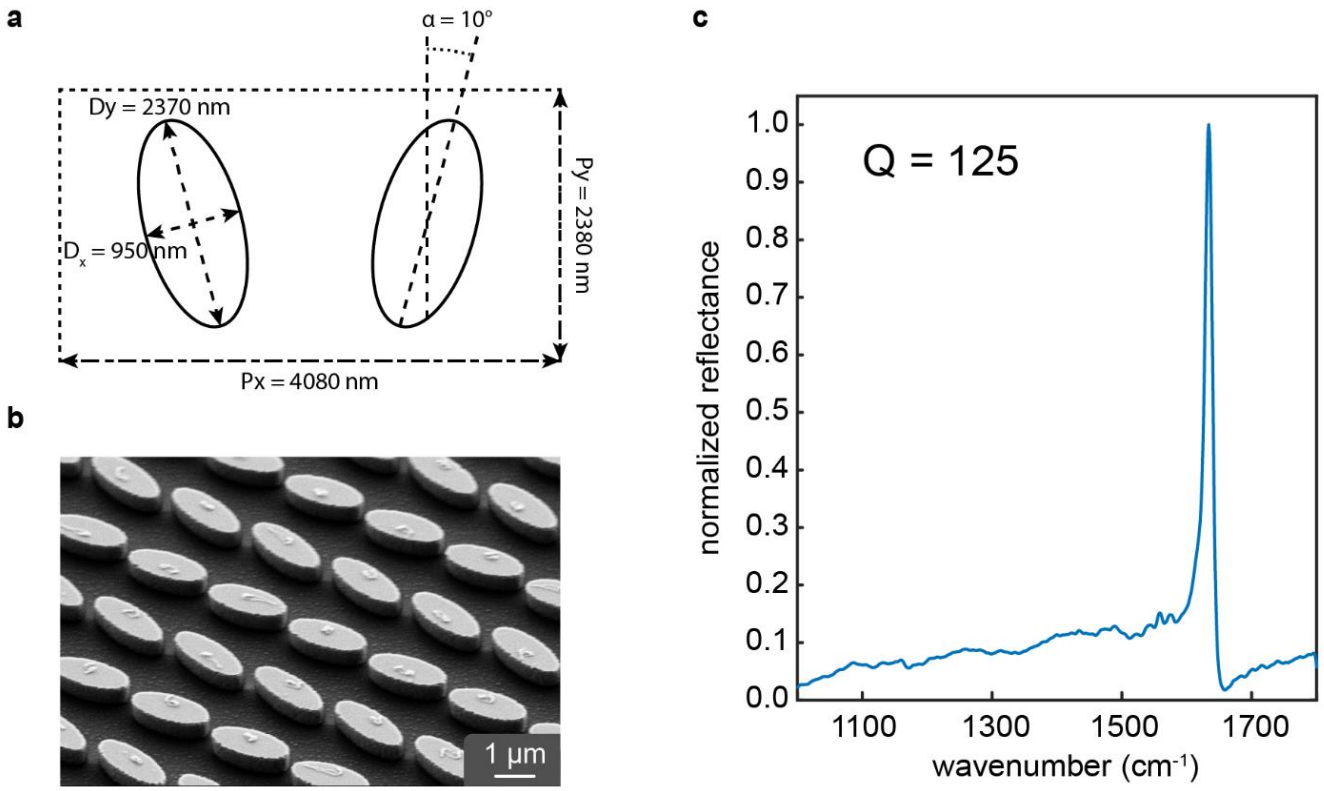

Figure S6: All-dielectric High-Q metasurfaces. **a**) High-Q metasurface resonator design parameters. **b**) Scanning electron micrograph of the DUV fabricated metasurface. **c**) Measured optical response confirms high-quality resonance with Q-factor of 125.

Silicon-based metasurfaces and HfO_2 free-standing membranes

Our fabrication method is versatile and compatible with different materials both for the metasurfaces and the membranes. For instance, it is not limited to only germanium and aluminum metasurfaces. The Al_2O_3 as a substrate material is compatible with various deposition methods and materials such as silicon[7], germanium, metal-oxides,[8] diamond,[9] and graphene[10]. Moreover, the ultra-thin membranes can also be realized with other metal-oxides. To illustrate this flexibility, here, we demonstrate Si-based metasurface on free-standing HfO_2 membranes. The fabrication process flow starts with 60 nm thick HfO_2 film deposition on Si wafer using the ALD method. Then a 700 nm thick polysilicon is deposited by low-pressure chemical vapor deposition (LPCVD) at 625 °C. The rest of the process remains the same as described in Figure 1a. The SEM of the fabricated metasurface is

displayed in Figure S7a, while the cross-section of the thin membrane-based metasurface is displayed in Figure S7b. The high-quality resonances are confirmed with mid-IR laser-based microscopy measurements (Figure S7c). The average quality factor of the metasurfaces in the spectral range from 1400 cm^{-1} to 1800 cm^{-1} is 130.

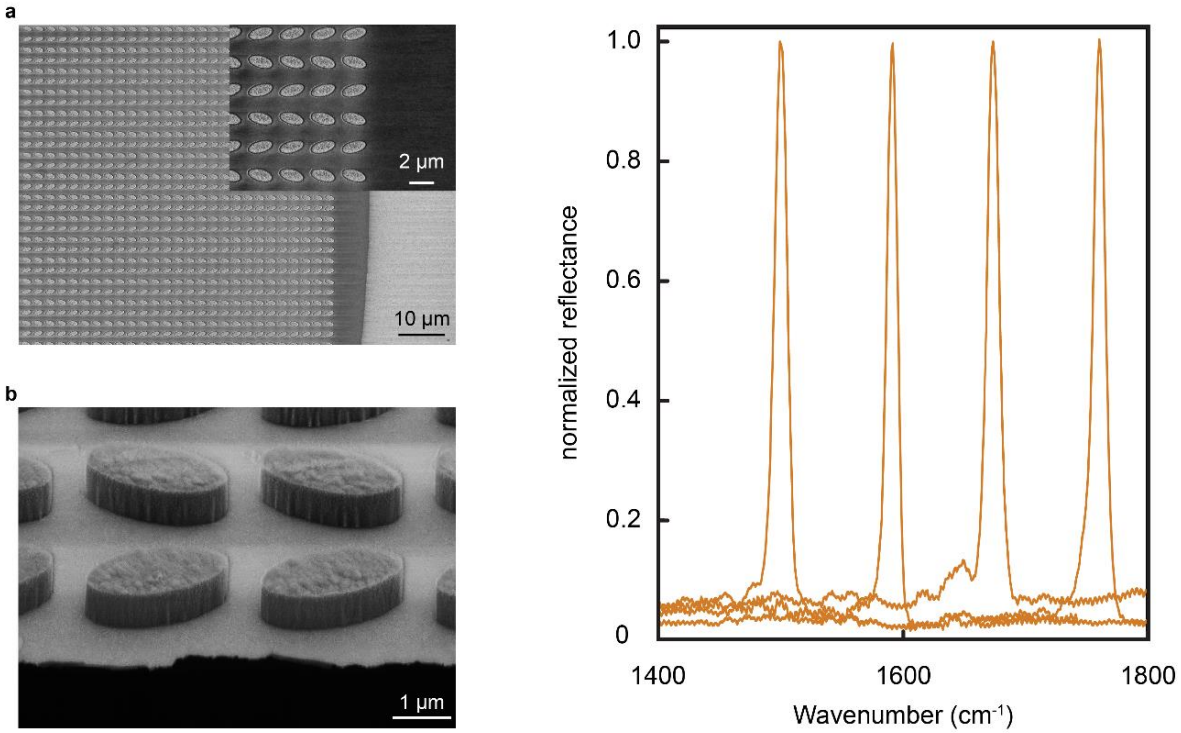

Figure S7: **Silicon-based metasurfaces on HfO_2 free-standing membranes**. **a**) SEM of polysilicon metasurface on free-standing HfO_2 membranes. **b**) Cross-section scanning electron micrograph of the DUV fabricated metasurface. **c**) Measured optical response of Si metasurfaces confirms background-free and high-quality resonances with Q-factors up to 130.

Metalens characterization

We characterized the metalenses using a quantum cascade laser-based mid-IR microscope (DRS Daylight solutions Spero). The tunable laser sources enabled measurements of the metalens spectral response, while the high precision microscope stage allowed to characterize the focusing profile along the light propagation axis with high spatial resolution. In order to avoid overexposing the sensitive microbolometer detector, we inserted a neutral density filter in the light path (ND 2.0), which attenuates the incoming light by a factor of 100. The measured focusing profile at a fixed laser wavelength of 6.5 µm along the propagation axis is displayed in Figure S8a. The beam profile at the focal plane shows strong focusing and completely circularly symmetric intensity distribution (Figure S8b). The measured focal length (f) of the metalens with a 350 µm radius (R) was 897 µm. Knowing the focal length and the diameter, one can calculate the numerical aperture of the metalens, which is NA = 0.364. The experimentally measured profile of the focal spot was compared to a theoretical Airy

disk pattern, see Figure S8c. The fitted Airy disk pattern shows a disk diameter of 22.2 µm, which corresponds to a diffraction-limited spot size for a lens with NA = 0.36.

Additionally, we evaluated the transmission efficiency and the focusing efficiency of the metalens. The experimentally measured transmission efficiency of the metalens is 90.3%, while the focusing efficiency is 70.4%. Here, the focusing efficiency was defined as the ratio between the total light power within the measured focal spot having a diameter of 22.2 µm with the total power of the incident light on the metalens. The focusing efficiency could be further improved by optimizing the nanofabrication parameters, such as optical dose during the DUV lithography step and dry etching parameters.

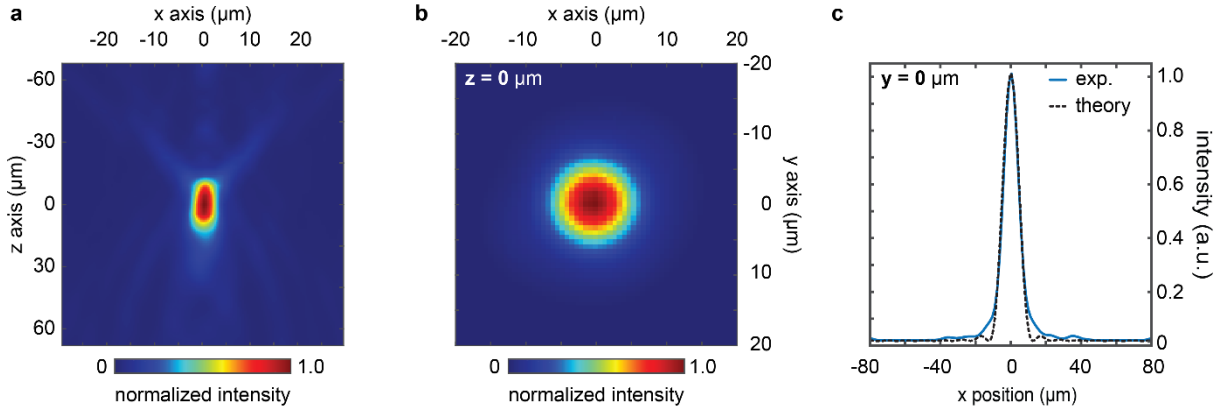

Figure S8: Metalens characterization. a) Focusing profile of the metalens along the zx-plane. **b**) Beam spot profile at the focal plane. **c**) The experimental data and its comparison to a theoretical Airy disk pattern, showing the focusing spot diameter of 22.2 µm.

Large area membrane-based metasurfaces

The main manuscript shows membrane-based metasurfaces with sizes up to 700 µm. Notably, the size of the membrane-based metasurfaces can be extended further. Figure S9a shows a micrograph of an experimentally realized metalens with a diameter of 1.1 mm. However, moving further to centimeter-scale metasurfaces would adversely affect the stability of the ultra-thin membranes and the yield of membrane-based metasurface nanofabrication. In order to overcome this size limitation, the membrane-based metasurfaces could be tiled together to form a large area metasurface see Figures S9b and S9c. Here the free-standing membranes could be suspended on narrow silicon bridges, which would allow to effectively realize centimeter-scale metasurfaces while maintaining low optical losses (Figure S9c).

To estimate the optical losses of the tiled metasurfaces, we need to calculate the ratio between the area of silicon-based connecting bridges (S_b) and the single hexagonal tile (S_t). The area of the

hexagonal polygon having equal side lengths (a) can be calculated using the following equation: $S_t = \frac{3\sqrt{3}}{2}a^2$. While the area of connecting bridges per one tile could be calculated as $S_b = wa \cdot d/2$, where w is the width of the connecting bridge. In the previous equation, the bridge width w is divided by a factor of 2 because the connecting bridges are shared between neighboring cells. If we assume the length of the hexagon side to be $a = 250\ \mu\text{m}$ and the bridge width $w = 10\ \mu\text{m}$, it gives the tile area of $S_t = 1.62 \cdot 10^5\ \mu m^2$ and area of the silicon-based connecting bridge of $S_b = 7.5 \cdot 10^3 \mu m^2$. Here the values a and w are chosen conservatively, where the side length a of 250 µm gives smaller hexagon area than the demonstrated metalens in Figure 3 and Figure S9a, while the connecting bridge width of 10 µm is similar to the ones for pixelated metasurfaces demonstrated in Figure 2 and Figure S3b.

To approximately estimate the optical losses, we calculate the ratio between the areas of the connecting bridges and the whole hexagonal tile ($S_b/S_t = 0.046$). It shows that if no light would pass through the silicon bridges, then we would lose less than 5% of light using tiled metasurfaces. Notably, this is a conservative estimate because the silicon is not opaque in the mid-IR, and the calculations did not take into account that there are no bridges needed for the outer border of the tiled metasurface.

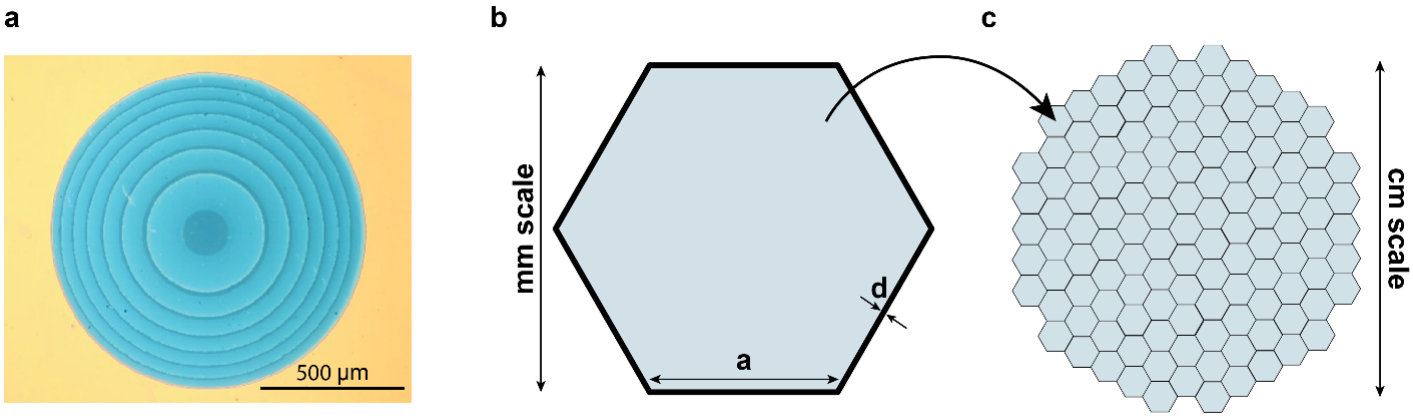

Figure S9: Large area membrane-based metasurfaces. a) Optical micrograph of a 1.1 mm large metalens. **b**) Schematic drawing of a hexagonal tile. **c**) Extended centimeter-scale metasurface composed of multiple tiles.

Birefringent metasurfaces

In order to induce birefringence properties into the metasurface, we broke the rotational symmetry of the Ge posts. Specifically, we chose elliptical posts as the meta-atoms and carefully tuned the ratio between its long and short axes. This symmetry breaking enables the control of the light polarization states. Figure S10a demonstrates the numerical simulation data of the optical phase delay when the light passes through the metasurface for different meta-atom post ellipticities at the operation

wavenumber of 1360 cm^{-1} corresponding to 7.35 μm. Specifically, the top part of Figure S10a shows the optical phase when the light is polarized along the y-axis while the bottom panel shows the case when the light is polarized along the x-axis. The transmittance properties of the metasurface with different post ellipticities are displayed in Figure S10b with light polarization along the y-axis at the top and polarization along the x-axis at the bottom. The optical phase difference between the two polarization states is shown in Figure S10c, while the average transmittance of both polarization states is displayed in Figure S10d.

Interestingly, in the phase difference map, we can find specific locations where the optical phase difference is 0.5 of the full 2π phase, meaning that it would turn the polarization by 90°. Therefore, the metasurface would perform as a λ/2 plate. The optical phase difference between the two polarization states can be obtained if the initial polarization of the light is 45° tilted compared to the x- and y-axis (Figure S10e). The light that passes through the metasurface has orthogonal polarization. We characterized the metasurface using the mid-IR laser-based microscope and an additional polarizer (analyzer) right after the metasurface (Figure S10e). If the analyzer is parallel to the initial polarization state, then there is almost no light going through the system (Figure S10f). However, if the analyzer is turned perpendicular to the initial light polarization, then we obtain 96% of light transmittance (Figure S10f left panel). The measured optical response of the birefringent metasurface is in excellent agreement with the simulation data.

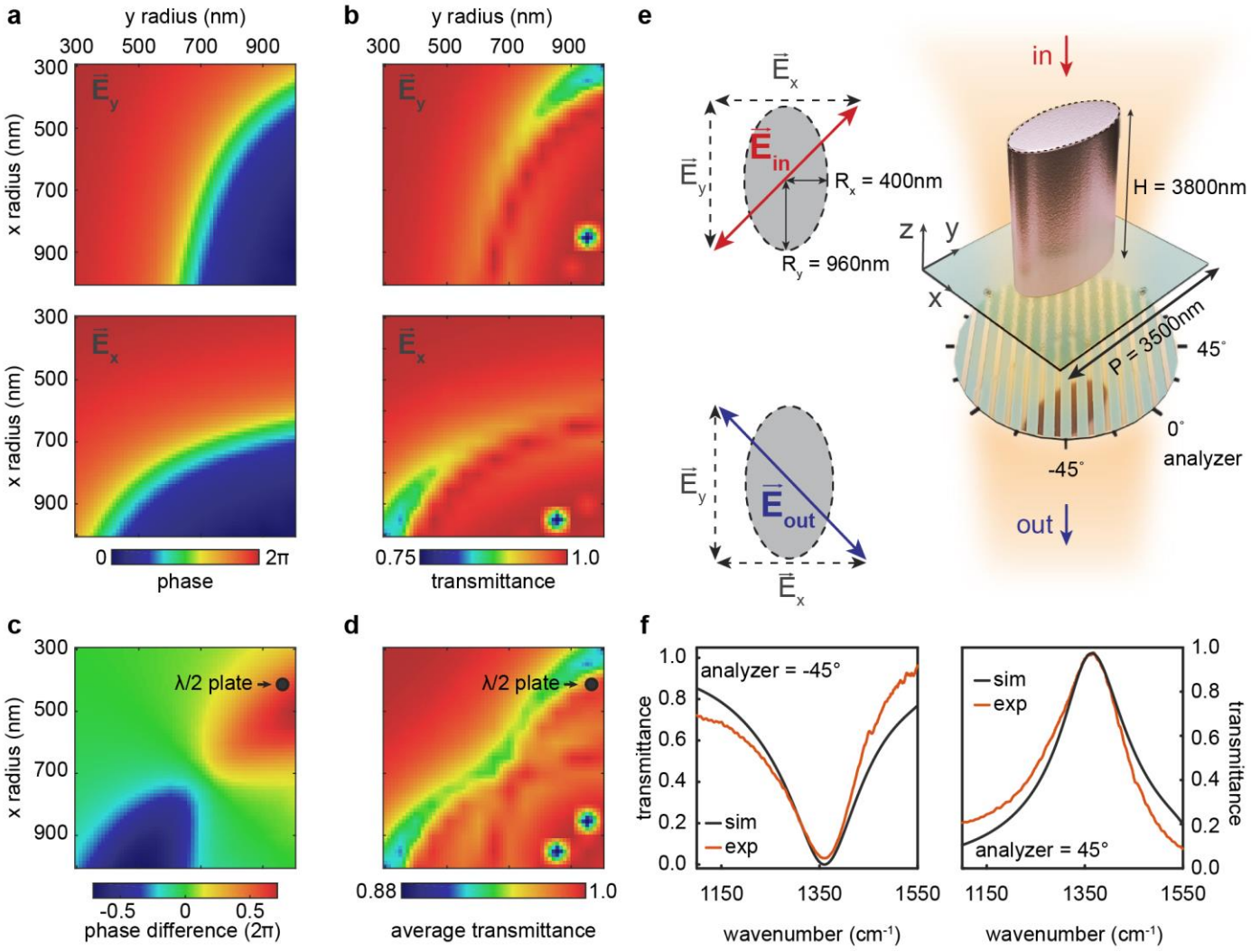

Figure S10: Birefringent metasurfaces. **a**) Optical phase for different post radiuses and polarization states. **b**) Birefringent metasurface transmittance for different post radiuses and polarization states. **c**) Phase difference between the two polarization states for different post radiuses. **d**) Average transmittance of the two polarization states. **e**) Sketch of the experimental setup and the birefringent metasurface unit cell. **f**) Comparison of the simulation and measurement data.

Numerical simulations of the plasmonic metasurface

We designed plasmonic metasurfaces for targeting the main absorption bands of proteins and lipids in aqueous solutions. To obtain the nanoantennas' precise dimensions, we performed numerical simulations by using commercial software (CST Microwave studio). The unit-cell consists of 5 nanoantennas, where the central antenna targets protein absorption bands near 1600 cm^{-1} (6.25 µm), while the four smaller antennas target the lipid absorption bands near 3000 cm^{-1} (3.33 µm). The specific nanoantenna shape and size are displayed in Figure S11a. The simulation and the experimental spectra are shown in Figure S11b. The resonance positions and intensities of the measured spectra are in very good agreement with the simulation data. The pronounced dips in the resonances near 1600 cm^{-1} and 3250 cm^{-1} are induced by the water infrared absorption bands.

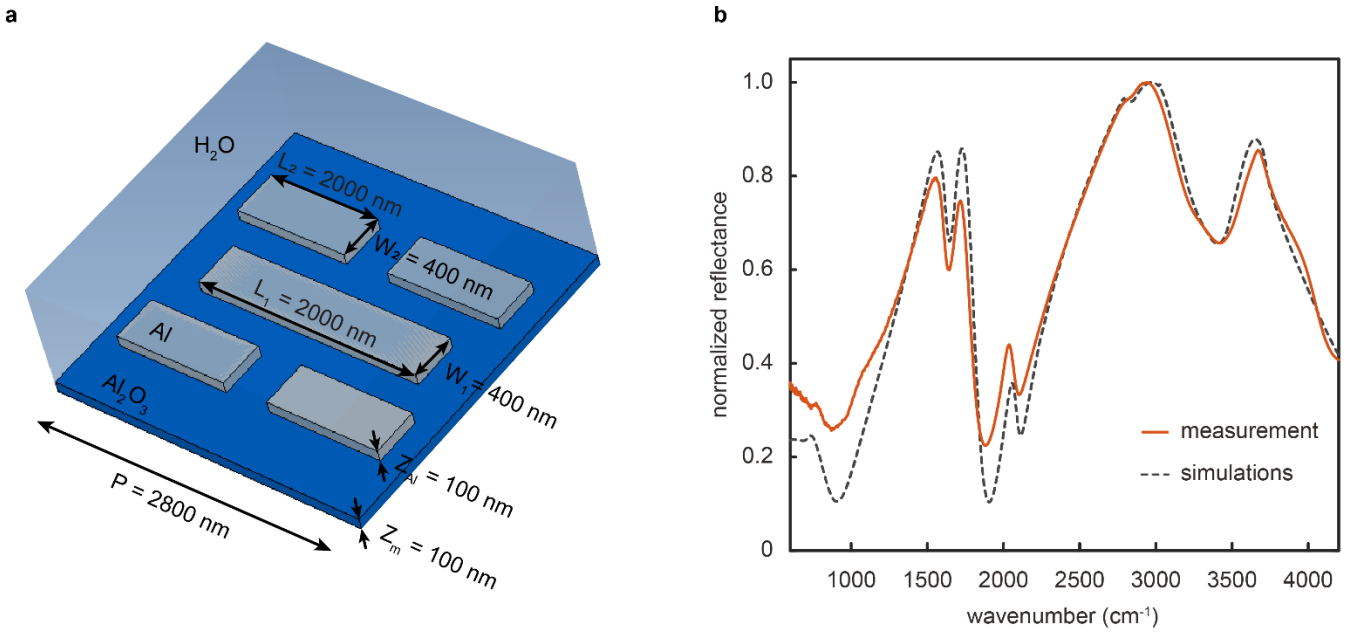

Figure S11: Numerical simulations of plasmonic metasurface. **a**) Multiresonant plasmonic metasurface design tuned for simultaneous lipid and protein biosensing. **b**) The simulated and experimentally measured reflectance when immersed in water.

Plasmonic biosensing

After fabrication, the plasmonic chips were exposed to UV light for 1 minute and then functionalized by immersion for 72 hours in 2.5 mM 11-Phosphonoundecanoic acid (PUA) dissolved in 1:1 IPA:H_2O. Contact angle measurements of water droplets on the chip surface before (Figure S12a) and after functionalization (Figure S12b) reveal a clear increase in hydrophobicity. The contact angle measurement data is in agreement with the values reported in the literature, therefore confirming the successful formation of a monolayer on the chip surface.[11] For the contact angle measurements, the activation of the carboxyl end groups was performed ex-situ by incubating the functionalized chip with 200 mM Sulfo-NHS (N-Hydroxysulfosuccinimide sodium salt, Sigma-Aldrich) / 50 mM EDC (N-(3-Dimethylaminopropyl)-N ´ -ethylcarbodiimide hydrochloride, Sigma-Aldrich) in MES buffer solution. The measured increase in hydrophilicity supports the successful formation of amine-reactive esters (Figure S12c). For the real-time biosensing measurements, the NHS/EDC activation is performed in-flow with a volume of 300 µL, as for the other analyte injections, i.e., 3 µM streptavidin (Thermo Fisher Scientific) in PBS and 1 mg·mL^{-1} biotinylated liposomes in PBS. The liposomes are prepared as follows: 95 %mol POPC (1-palmitoyl-2-oleoyl-glycero-3-phosphocholine, Avanti Polar Lipids, Inc.) and 5 %mol Biotinyl PE (1,2-dipalmitoyl-sn- glycero-3-phosphoethanolamine-N-(biotinyl), Avanti Polar Lipids, Inc.) lipids are mixed in chloroform, dried overnight, resuspended in PBS and then extruded

19x through a 100 nm pore-size polycarbonate filter. The running buffer solution is PBS, which continuously flows at 30 µL·min^{-1}. For the data processing and analysis, we first convert the reflectance R to absorption spectra using the spectroscopic formula $-10^3 \cdot \log_{10}(R/R_0)$, where R_0 corresponds to the averaged reflectance spectra of the baseline before analyte injection. The absorption spectra are then baseline-corrected by subtracting an asymmetric least squares (ALS) fit,[12]. Next, multiple linear regression is carried out with these spectra to extract analyte coefficients which are smoothed by ALS fitting.

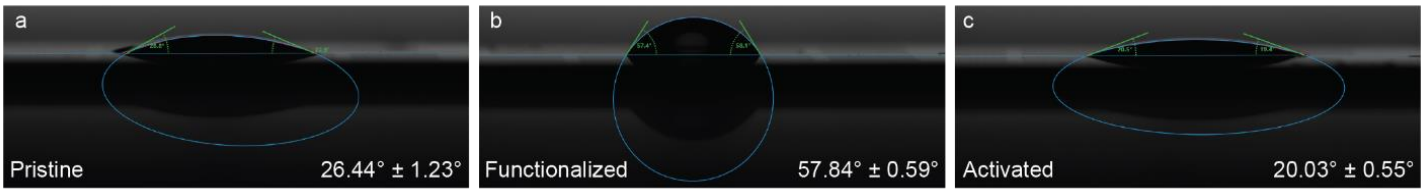

Figure S12: Contact angle measurement images of membrane chip surface. a) Before functionalization, **b**) after functionalization, and **c**) after end group activation with NHS/EDC. For each case, twenty measurements were performed, and the corresponding average contact angle and its standard deviation are indicated on the bottom right.

References

1. Yang, Q. *et al.* Mie-Resonant Membrane Huygens' Metasurfaces. *Adv. Funct. Mater.* **30**, 1–7 (2020).

2. Decker, M. *et al.* High-Efficiency Dielectric Huygens' Surfaces. *Adv. Opt. Mater.* (2015) doi:10.1002/adom.201400584.

3. Koshelev, K., Lepeshov, S., Liu, M., Bogdanov, A. & Kivshar, Y. Asymmetric metasurfaces with high-Q resonances governed by bound states in the continuum. *Phys. Rev. Lett.* **121**, 193903 (2018).

4. Tittl, A. *et al.,* Imaging-based molecular barcoding with pixelated dielectric metasurfaces. *Science.* **360**, 1105–1109 (2018).

5. Leitis, A. *et al.,* Angle-multiplexed all-dielectric metasurfaces for broadband molecular fingerprint retrieval. *Sci. Adv.* **5**, eaaw2871 (2019).

6. Oh, D. K. *et al.* Nanoimprint lithography for high-throughput fabrication of metasurfaces. *Front. Optoelectron.* (2021) doi:10.1007/s12200-021-1121-8.

7. Arbabi, A., Briggs, R. M., Horie, Y., Bagheri, M. & Faraon, A. Efficient dielectric metasurface

collimating lenses for mid-infrared quantum cascade lasers. *Opt. Express* **23**, 33310 (2015).

8. Chen, Z. *et al.* ZnO thin film deposition on sapphire substrates by cemical vapor deposition. *Mater. Res. Soc. Symp. Proc.* **1167**, 89–94 (2009).

9. May, P. W. *et al.* Deposition of diamond films on sapphire: studies of interfacial properties and patterning techniques. *Diam. Relat. Mater.* **3**, 1375–1380 (1994).

10. Shan, J., Sun, J. & Liu, Z. Chemical Vapor Deposition Synthesis of Graphene over Sapphire Substrates. *ChemNanoMat* **7**, 515–525 (2021).

11. Zhang, B. *et al.* Surface functionalization of zinc oxide by carboxyalkylphosphonic acid self-assembled monolayers. *Langmuir* **26**, 4514–4522 (2010).

12. Eilers, P., Report, H. B.-L. U. M. C. & 2005, undefined. Baseline correction with asymmetric least squares smoothing.